

Topological phase singularities in atomically thin high-refractive-index materials

Georgy Ermolaev

Moscow Institute of Physics and Technology, <https://orcid.org/0000-0002-0895-818X>

Kirill Voronin

MIPT <https://orcid.org/0000-0002-8911-1166>

Denis Baranov

Moscow Institute of Physics and Technology <https://orcid.org/0000-0002-8071-1587>

Vasyl Kravets

University of Manchester

G. Tselikov

Moscow Institute of Physics and Technology <https://orcid.org/0000-0002-6664-7881>

Yury Stebunov

University of Manchester

Dmitry Yakubovsky

Moscow Institute of Physics and Technology

Sergey Novikov

Moscow Institute of Physics and Technology

Andrey Vyshnevyy

Moscow Institute of Physics and Technology

Arslan Mazitov

Moscow Institute of Physics and Technology <https://orcid.org/0000-0002-6549-7324>

Ivan Kruglov

Dukhov Research Institute of Automatics

Sergey Zhukov

Moscow Institute of Physics and Technology

Roman Romanov

Moscow Institute of Physics and Technology

Andrey Markeev

Moscow Institute of Physics and Technology

Aleksey Arsenin

Moscow Institute of Physics and Technology

Konstantin Novoselov

National University Singapore <https://orcid.org/0000-0003-4972-5371>

Alexander Grigorenko

University of Manchester

Valentyn Volkov (✉ vsv.mipt@gmail.com)

Moscow Institute of Physics and Technology <https://orcid.org/0000-0003-2637-1371>

Article

Keywords: Atomically thin transition metal dichalcogenides, photonics, topological phase singularities

Posted Date: August 26th, 2021

DOI: <https://doi.org/10.21203/rs.3.rs-829403/v1>

License: © ⓘ This work is licensed under a Creative Commons Attribution 4.0 International License.

[Read Full License](#)

Version of Record: A version of this preprint was published at Nature Communications on April 19th, 2022. See the published version at <https://doi.org/10.1038/s41467-022-29716-4>.

Topological phase singularities in atomically thin high-refractive-index materials

Georgy Ermolaev[†],¹ Kirill Voronin[†],^{1,2} Denis G. Baranov,¹ Vasyl Kravets,³ Gleb Tselikov,¹ Yury Stebunov,⁴ Dmitry Yakubovsky,¹ Sergey Novikov,¹ Andrey Vyshnevyy,¹ Arslan Mazitov,^{1,5} Ivan Kruglov,^{1,5} Sergey Zhukov,¹ Roman Romanov,⁶ Andrey M. Markeev,¹ Aleksey Arsenin,¹ Kostya S. Novoselov,^{4,7,8} Alexander N. Grigorenko,³ and Valentyn Volkov¹

¹Center for Photonics and 2D Materials, Moscow Institute of Physics and Technology, Dolgoprudny 141700, Russia.

²Skolkovo Institute of Science and Technology, Moscow 121205, Russia.

³Department of Physics and Astronomy, University of Manchester, Manchester M13 9PL, UK.

⁴National Graphene Institute (NGI), University of Manchester, Manchester M13 9PL, UK.

⁵Dukhov Research Institute of Automatics (VNIIA), Moscow 127055, Russia.

⁶National Research Nuclear University MEPhI (Moscow Engineering Physics Institute), Moscow 115409, Russian Federation.

⁷Department of Materials Science and Engineering, National University of Singapore, Singapore 03-09 EA, Singapore.

⁸Chongqing 2D Materials Institute, Chongqing 400714, China.

e-mail: volkov.vs@mipt.ru

19 **ABSTRACT**

20 Atomically thin transition metal dichalcogenides (TMDCs) present a promising platform for
21 numerous photonic applications due to excitonic spectral features, possibility to tune their
22 constants by external gating, doping, or light, and mechanical stability. Utilization of such
23 materials for sensing or optical modulation purposes would require a clever optical design, as by
24 itself the 2D materials can offer only a small optical phase delay – consequence of the atomic
25 thickness. To address this issue, we combine films of 2D semiconductors which exhibit excitonic
26 lines with the Fabry-Perot resonators of the standard commercial SiO₂/Si substrate, in order to
27 realize topological phase singularities in reflection. Around these singularities, reflection spectra
28 demonstrate rapid phase changes while the structure behaves as a perfect absorber. Furthermore,
29 we demonstrate that such topological phase singularities are ubiquitous for the entire class of
30 atomically thin TMDCs and other high-refractive-index materials, making it a powerful tool for
31 phase engineering in flat optics. As a practical demonstration, we employ PdSe₂ topological
32 phase singularities for a refractive index sensor and demonstrate its superior phase sensitivity
33 compared to typical surface plasmon resonance sensors.

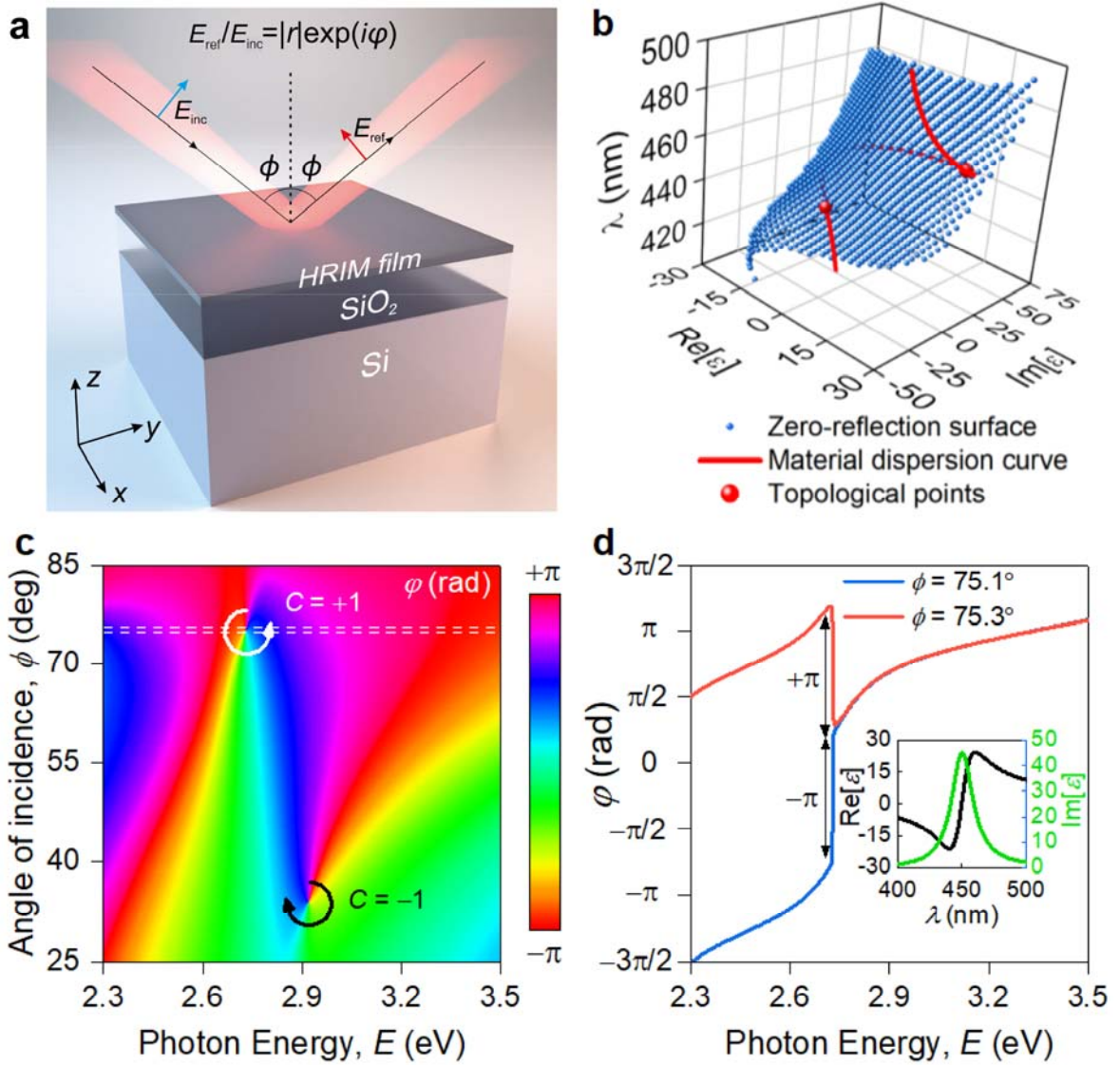
34 **INTRODUCTION**

35 Optical waves carry energy and information encoded in their electric field amplitude, phase, and
36 polarization. While light field amplitude is still used the most in various applications, optical
37 phase manipulation could lie in the core of next-generation information technologies.¹⁻³
38 Generally, the phase acquired by light upon reflection, scattering, or transmission varies rapidly
39 when the amplitude of the light (reflected, scattered, or transmitted, respectively) goes to zero.⁴⁻⁷
40 Reflection zeros can be encountered in the effect of plasmonic blackbody,⁸ perfect absorption,^{9,10}
41 coherent perfect absorption,¹¹ Brewster angle^{12,13} or more sophisticated examples of zero-
42 reflection modes.^{5,14} Such zeros of response function always reveal phase singularities^{4,5,15,16}
43 which are accompanied by a non-trivial topological charge $C = \frac{1}{2\pi} \oint_{\gamma} \text{grad}(\varphi) ds$, where φ is the

44 response function phase while the integration is performed along a path γ enclosing the singular
45 point (zero response point) in two-dimensional parameter space.^{5,15,16}

46 To demonstrate how phase singularities associated with zero-reflection can be topologically
47 protected, let us consider light reflection from a planar structure shown in Figure 1a, where an
48 atomically thin layer of a high-refractive index material (HRIM) is placed on top of SiO₂/Si
49 substrate. For a given thickness of HRIM film, an angle of incidence (ϕ), the photon energy (E),
50 and polarization, reflection from the structure can be made exactly zero by calculating
51 appropriate values for the dielectric permittivity of the HRIM film ($\text{Re}(\epsilon)$ and $\text{Im}(\epsilon)$), which can
52 be always found by the nature of Fresnel coefficients for the structure.¹⁷ When we change an
53 angle of incidence and a photon energy in some range, a zero-reflection surface will appear, see
54 the blue surface in Figure 1b. Any point on the zero-reflection surface corresponds to zero-
55 reflection (at some angle of incidence and light wavelength) for the studied structure. Now we
56 plot an actual dependence of the dielectric constants HRIM on the photon energy on the same
57 graph (the so-called material dispersion curve), see the red line in Figure 1b. In the presence of a
58 reasonably large resonance feature, this curve would look like a spiral in the space of (E , $\text{Re}(\epsilon)$
59 and $\text{Im}(\epsilon)$) and hence will inevitably cross the surface of zero-reflection as shown in Figure 1b.
60 For a Lorentz resonance feature,¹⁷ there will be two intersection points between the material
61 dispersion curve and the zero-reflection point resulting in two zeros of reflection from the
62 structure in Figure 1a. It is necessary to stress that these intersection points are protected by the
63 Jordan theorem.^{5,6} Indeed, minor variations of the material dispersion curve caused by material
64 imperfections will not change the relative alignment of the curve and the zero-reflection surface
65 and cannot lead to disappearance of the zero-reflection points which lead to the idea of
66 topological darkness.^{5,6} Our structure relies on the atomic flatness of the interfaces and on the
67 sharp changes of the refractive indexes, which offer a non-trivial possibility to realize zero-
68 reflection and topological singularities for atomically thin layers in this structure at visible light,
69 which was never achieved before.

70 Zero-reflection implies perfect absorption of the light that falls onto the discussed structure
71 (as transmission through the silicon substrate should be zero). Zero-reflection entails phase
72 singularity due to the singular nature of light phase at zero light amplitude (where the phase of
73 light is not defined). Figure 1c represents the map of the p-polarized wave reflection phase in
74 space of E and ϕ , which contains two phase singularities corresponding to the zero-reflection
75 points with topological charges equal to -1 and $+1$ (the topological points of Figure 1b). Of
76 immediate interest is a bifurcation behavior of optical phase in the vicinity of topological point
77 (Figure 1d). In other words, phase reveals abrupt $\pm\pi$ -jumps near a zero-reflection when plotted as
78 a function of wavelength for a fixed incidence angle close to a phase singularity. It gives an
79 indispensable degree of freedom for efficient phase manipulation.



80

81 **Figure 1. Topology of the reflection phase near the singular point.** **a** Schematics of
 82 generalized structure for observation of phase singularities, arising from interaction of Fabry-
 83 Perot resonator's (280 nm SiO₂/Si) modes with ultrathin films of HRIM. **b** Phase singularity
 84 point arises when zero-reflection surface of the system HRIM/SiO₂/Si intersects with the
 85 material dispersion curve of HRIM. **c** In close vicinity of zero-reflection points, phase becomes
 86 singular and acquires topological charge $C = -1$ or $+1$, corresponding to -2π or $+2\pi$ phase
 87 round-trip accumulation. **d** Phase has opposite π -gradient for angles slightly above and below
 88 singular point (dashed lines in panel (c)) giving rise to topological charge with 2π round-trip

89 around zero-reflection point. The inset is a dielectric permittivity of the model HRIM used for
90 calculation of (b) and (c).

91 The most exciting consequence of such optical phase control is the realization of “flat optics”
92 paradigm – flexible manipulation of the optical wavefront by an arrangement of subwavelength
93 planar objects to shape the desired phase pattern.^{1,18–20} Such “flat optics” paradigm enables
94 miniaturized metalenses^{21–23} and meta-holograms,^{24–26} and two-dimensional (2D) materials²⁷
95 such as graphene,²⁸ transition metal dichalcogenides,²⁹ and organic semiconductors³⁰ provide an
96 excellent platform for implementation of these components. Although these works constitute an
97 important step towards truly flat optics, the efficiency of current devices is limited by the
98 fundamental constraints. Indeed, the typical wavefront manipulation applications require that the
99 phase accumulated by a light wave upon interaction with such a device can be tuned at least
100 within the range of π . However, in the monolayer limit ($t \sim 0.65$ nm and $n \sim 4$) for visible light
101 ($\lambda \sim 600$ nm), the resulting phase delay, which is approximately determined by the optical
102 thickness of the 2D material layer, is only about 0.01π . Consequently, finding new ways to
103 induce strong optical phase variations in atomically thin structures is vital for flat optics.

104 Here, we demonstrate a platform for efficient optical phase manipulation presented by
105 atomically thin high-refractive-index materials (HRIMs) that often possess excitonic resonances.
106 We experimentally observe zero-reflection, phase singularities, and rapid phase variation of
107 reflected light in extremely thin layers (down to single monolayer!) of PdSe₂, graphene, MoS₂,
108 and WS₂ films placed on SiO₂/Si substrate. Combined theoretical and experimental analysis
109 indicates that the zero-reflection points are accompanied by a non-trivial topological charge. We
110 derive an analytical condition for such points to occur in layered structures containing optically
111 thin films and predict the occurrence of these points in structures containing a broader family of
112 atomically thin HRIMs and substrates. The observed effect is highly robust and does not require
113 complicated fabrication steps guaranteeing its reproducibility and reliability. In contrast to

114 optical darkness observed for dielectric materials and multilayers which disappears with layer
115 irregularities (e.g., at Brewster angle conditions) the effect is topologically protected. It can be
116 used in numerous applications, including label-free bio- and chemical sensing, photo-detection
117 and photo-harvesting, perfect light absorption in 2D monolayers, quantum communication and
118 security. As a practical application of this platform, we demonstrate a refractive index sensor that
119 can rival modern plasmon resonance-based counterparts.³¹ Therefore, our phase engineering
120 approach as a whole offers an advanced tool for current and next-generation 2D flat optics.

121 **RESULTS**

122 **Phase singularities in reflection**

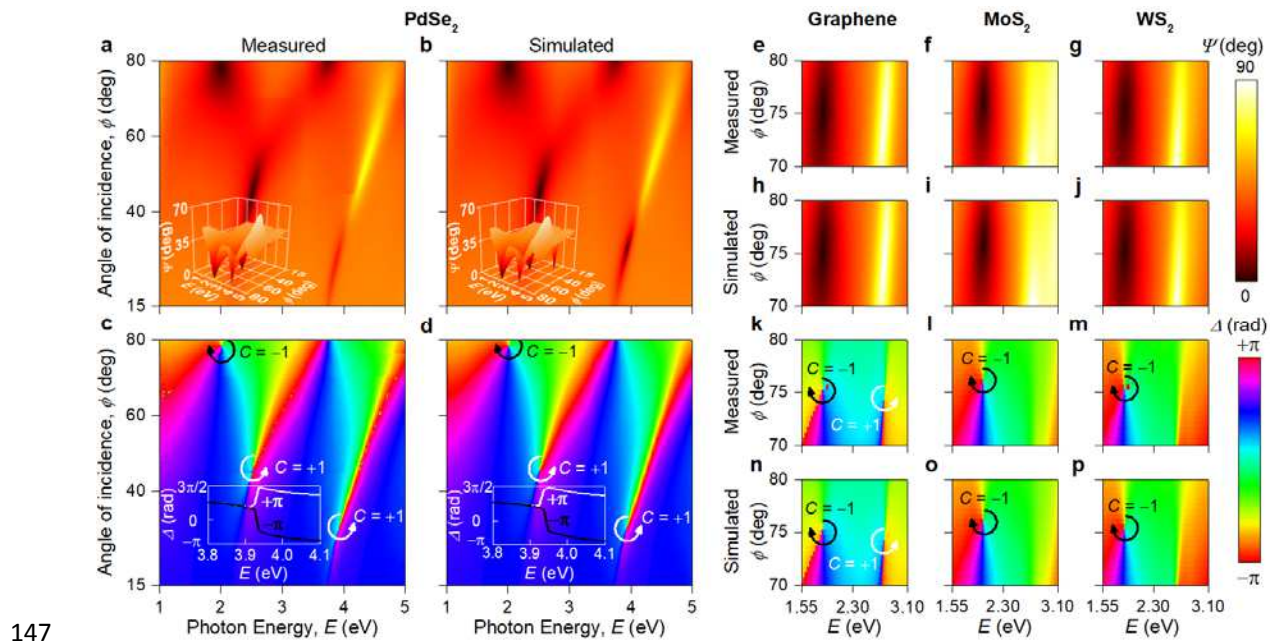
123 To examine topological properties of the light reflectance from thin HRIM films placed on
124 SiO₂/Si substrates, we utilized spectroscopic ellipsometry (Methods). The unique advantage of
125 this technique is the simultaneous determination of reflection amplitude and phase in terms of
126 the ellipsometric parameters Ψ and Δ , which are defined through the complex reflection ratio ρ :³²

$$\rho = \tan(\Psi)e^{i\Delta} = \frac{r_p}{r_s} \quad (1)$$

127 where r_p and r_s are the amplitude reflection coefficients of p- and s-polarized plane waves.
128 Therefore, ellipsometry provides us with the information not only about the reflected light
129 amplitude, but also about the light phase.

130 Unexpectedly, we found that light reflection measured from 5.1 nm thick PdSe₂ as well as for
131 monolayers of graphene, MoS₂, and WS₂ on SiO₂/Si substrate showed a number of zero-
132 reflection points as explained in Figure 2. Remarkably, the measured amplitude parameter Ψ in
133 Figure 2a is in excellent agreement with the simulated spectrum in Figure 2b calculated using the
134 transfer-matrix method.³³ However, the spectra of Ψ alone do not definitively indicate if an exact
135 zero was attained in reflection at the position of any of Ψ dips. This can be deduced from the
136 behavior of relevant phase which was measured using spectroscopic ellipsometry (phase Δ). The

137 angle-dependent spectrum of the measured ellipsometric phase Δ in Figure 2c and d clearly
 138 indicates that the reflected phase is undefined in the vicinity of certain points in the energy-
 139 incidence angle parameter space and possesses non-trivial topological charge C . These points are
 140 phase singularities, which can occur if and only if the response function (reflection in our case)
 141 takes zero magnitude at that point. Figure 2 reveals three such phase singularities for PdSe₂, two
 142 for graphene, and one for MoS₂ and WS₂ monolayers. Most of these phase singularities are
 143 associated with $\Psi = 0^\circ$ (equivalently $\rho = 0$ and, hence, $r_p = 0$), whereas one for graphene has
 144 $\Psi = 90^\circ$ (equivalently $\rho = \infty$ or $r_s = 0$). Simulated angle-dependent spectrum of Δ in Figure 2
 145 again demonstrates remarkable agreement with the experimental data, correctly predicting
 146 spectral positions of all phase singularities.



148 **Figure 2. Experimental observation of phase singularities.** **a, c** Experimental and **b, d**
 149 simulated ellipsometric parameters Ψ (amplitude) and Δ (phase) for PdSe₂ (5.1 nm)/SiO₂(280
 150 nm)/Si. The insets in panels (a) and (b) are their 3D view. The insets in panels (c) and (d) are
 151 phase behavior for incidence angles slightly above ($\phi = 30.5^\circ$) and below ($\phi = 30^\circ$) topological
 152 zero. **e-g, k-m** Experimental and **h-j, n-p** simulated Ψ and Δ for graphene, MoS₂, and WS₂ on
 153 SiO₂/Si. In close vicinity of topological points, phase becomes singular and acquires topological

154 charge $C = -1$ or $+1$. Optical constants of PdSe₂ for simulations are taken from Figure 3k.
 155 Meanwhile optical constants for graphene, MoS₂, and WS₂ were adopted from several
 156 reports.^{34,35}

157 Previous works⁴⁻⁶ realized these topological phase singularities only in metallic
 158 nanostructures through careful engineering of optical properties of nanostructured materials.
 159 Later, singular phase behavior was achieved in simple plasmonic heterostructures³⁶ where thin
 160 layers of metals (~20nm) and dielectric were used to generate zero reflection and phase
 161 singularities. Figure 2 proves that the heterostructure approach is quite general and could be
 162 realized even for 2D materials with ultimate atomic thickness in the simplest structure – 2D
 163 material/SiO₂/Si. The reason for this counterintuitive result is a rapid dielectric function variation
 164 (for example, due to excitons in TMDCs) in atomically thin HRIM. This rapid variation
 165 guarantees intersection with the zero-reflection surface (Figure 1b). Note that a thick layer is
 166 unsuitable for this purpose because absorption in that layer will prohibit interaction with the
 167 substrate's Fabry-Perot resonances.

168 To predict the position zero-reflection points for p- and s-polarized reflection in our structure
 169 shown in Figure 1a, we derived analytical expressions for the permittivities ε_p and ε_s of a thin
 170 film placed on a dielectric substrate which would result in the absence of the reflection for p- and
 171 s-polarized light, respectively (Supplementary Note 1):

$$\varepsilon_p = \frac{1}{k_0 t} \left(\frac{i\varepsilon_1}{q_{1z}} + \frac{\varepsilon_2}{q_{2z}} \frac{\frac{\varepsilon_3}{q_{3z}} - \frac{i\varepsilon_2}{q_{2z}} \tan(k_{2z}d)}{q_{3z} \tan(k_{2z}d) + \frac{i\varepsilon_2}{q_{2z}}} \right) \quad (2)$$

$$\varepsilon_s = \frac{1}{k_0 t} \left(iq_{1z} + q_{2z} \frac{q_{3z} - iq_{2z} \tan(k_{2z}d)}{q_{3z} \tan(k_{2z}d) + iq_{2z}} \right) \quad (3)$$

172 where t and d are thicknesses of the high-refractive-index material and dielectric layer
 173 respectively; ε_1 , ε_2 , and ε_3 are the dielectric permittivity of top halfspace, dielectric layer and
 174 bottom halfspace, in our case, that is air, SiO₂, and Si, respectively; $q_{iz} = k_{iz}/k_0 =$

175 $\sqrt{\varepsilon_i - \varepsilon_1 \sin^2(\phi)}$ is the normalized z-component (perpendicular to layers) of the wavevector in
 176 medium number i , $k_0 = \omega/c$, ω is the frequency, c is the speed of light, and ϕ is the angle of
 177 incidence. If the bottom halfspace is filled with a perfect electric conductor, the expressions can
 178 be simplified greatly to:

$$\varepsilon'_p = \frac{\varepsilon_2 \cot(k_{2z}d)}{q_{2z}k_0t} \quad \varepsilon''_p = \frac{\varepsilon_1}{k_{1z}t} \quad (4)$$

$$\varepsilon'_s = \frac{q_{2z} \cot(k_{2z}d)}{k_0t} \quad \varepsilon''_s = \frac{q_1}{k_0t} \quad (5)$$

179 where $\varepsilon'_{p,s}$ and $\varepsilon''_{p,s}$ are the real and imaginary parts of dielectric permittivity $\varepsilon_{p,s}$.

180 Equations (2) and (3) define a zero-reflection surface in the parameter space of wavelength,
 181 real and imaginary parts of the permittivity (λ , $\text{Re}[\varepsilon]$ and $\text{Im}[\varepsilon]$, respectively). Intersections of
 182 the material dispersion curve in this parameter space with the zero-reflection surface of the
 183 system (thin film of HRIM/SiO₂/Si) define zero-reflection points for the particular material of
 184 the film, as shown in Figure 1b. The topology of mutual arrangement of the curve and the
 185 surface underlies the robustness of the zero-reflection effect to external perturbations (roughness,
 186 temperature change, etc.). If a perturbation is introduced to the thin film, a displacement of the
 187 material dispersion curve and/or the zero-reflection surface will only result in a shift of the zero-
 188 reflection point in the parameter space, but will not lead to its disappearance (Figure 1b). This
 189 argument is in line with non-trivial topological charges of the observed phase singularities: small
 190 changes in the parameters of the system cannot lead to a change in the phase round-trip around a
 191 point, since it is an integer of 2π , thus making the zero-reflection point topologically protected.³⁷

192 Spectral positions of topological phase singularities can be controlled by either the thickness
 193 or the dielectric permittivity of the material. The derived analytical expressions allow us to
 194 generalize the effect of phase singularities to other high-refractive-index materials
 195 (Supplementary Note 2). Hence, the effect of rapid phase change is universal for all atomically

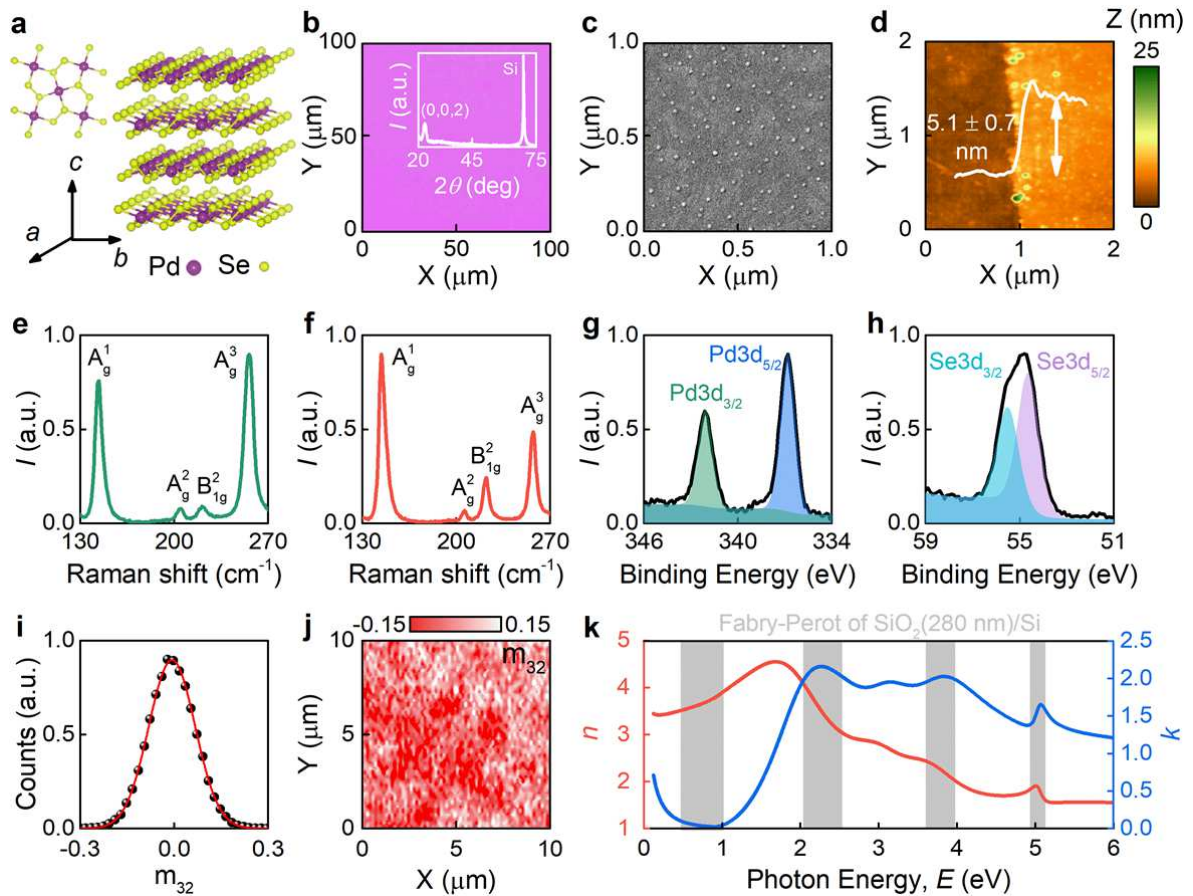
196 thin materials and substrates. It allows us hereafter to focus on PdSe₂, which demonstrates rich Ψ
197 and Δ spectra with a series of peaks and dips in Figure 2a-b. We begin with a detailed
198 characterization of PdSe₂ film, and then switch to unique applications and features of topological
199 phase gradient.

200 **Morphological and optical study of PdSe₂**

201 PdSe₂ thin films were prepared through chemical vapor deposition (CVD)³⁸ resulted in a uniform
202 sample as confirmed by representative optical and scanning electron microscopy (SEM) images
203 in Figure 3b-c. X-ray diffraction (XRD) spectrum showed pronounced peak in Figure 3b
204 validating the high crystallinity of the film.³⁹ Next, we validated the material's purity by X-ray
205 photoemission spectroscopy (XPS) in Figure 3g-h. It shows that Se:Pd atomic concentration ratio
206 equals 1.92, close to the expected value of 2. Additionally, Raman spectra in Figure 3e-f have
207 characteristic phonon modes A_g^1 , A_g^2 , B_{1g}^2 , and A_g^3 inherent to PdSe₂ with puckered pentagonal
208 crystal structure presented in Figure 3a.⁴⁰ This crystal configuration naturally has high
209 geometrical and, therefore, high optical anisotropy (see Supplementary Note 3).^{41,42}

210 To investigate anisotropic optical response, we measured Mueller matrices (Methods), which
211 nonzero off-diagonal elements relate to sample anisotropy (see Supplementary Note 3).
212 Interestingly, Mueller matrix' elements vary from point to point, as seen from Figure 3i-j.
213 Conceivably, it comes from the random growth during the CVD synthesis since Mueller
214 matrices' values in Figure 3i follow Gaussian law for random numbers. A similar random local
215 anisotropic response is observed by polarized optical microscopy and Raman spectroscopy
216 (Supplementary Note 3). Hence, at a macroscopic scale, our PdSe₂ layer exhibits an isotropic
217 dielectric response. It allowed us to investigate optical constants by classical ellipsometric and
218 reflectance measurements (see Supplementary Note 3) using the isotropic model for PdSe₂ with
219 5.1 nm thickness obtained by atomic force microscopy (AFM) in Figure 3d. The resulting
220 broadband dielectric function is presented in Figure 3k. As expected, PdSe₂ has pronounced

221 excitonic peaks⁴³ and a metallic Drude response caused by p-doping revealed by XPS (see
 222 Supplementary Note 3). Note that excitonic peaks of PdSe₂ align with Fabry-Perot resonances of
 223 the standard SiO₂ (280 nm)/Si substrate, making system PdSe₂/SiO₂(280 nm)/Si promising for
 224 enhancement of the PdSe₂ optical response.



225

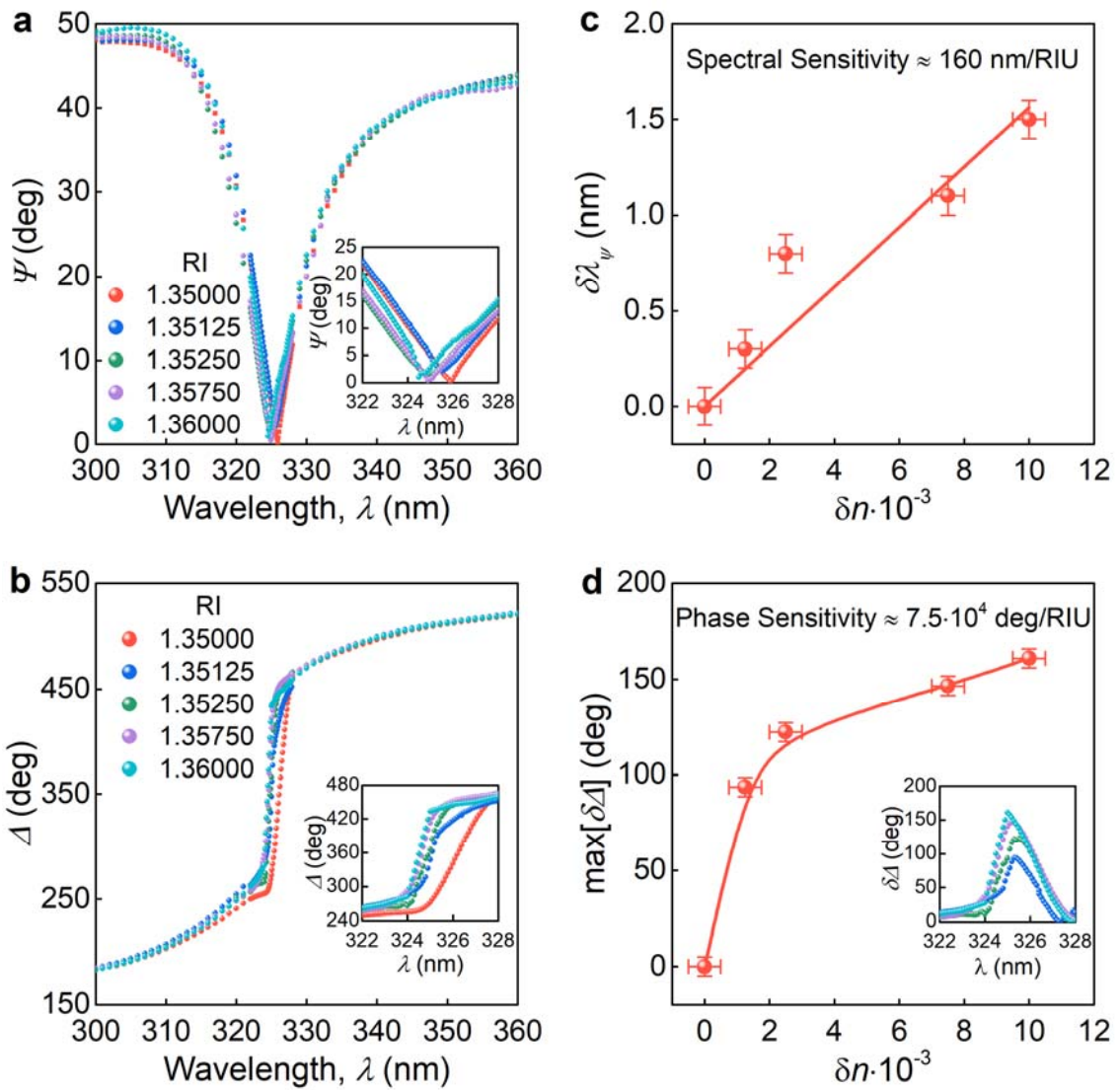
226 **Figure 3. Characterization of PdSe₂.** **a** Schematic illustration of PdSe₂ crystal structure. **b**
 227 Optical image of the sample. The inset shows PdSe₂ XRD diffraction pattern with pronounced
 228 peaks corresponding to the (0,0,2) crystal plane. Another peak is from Si substrate. **c** SEM image
 229 of the film. Small dots are seeding promoters for CVD growth. **d** AFM topography gives 5.1 nm
 230 film thickness. **e-f** Raman spectrum of PdSe₂ at excitation wavelengths $\lambda = 532$ nm (green line)
 231 and 632.8 nm (red line). **g-h** XPS spectra of PdSe₂. **i-j** Relative frequency and map of m_{32} (off-
 232 diagonal element of Mueller Matrix), indicating an anisotropic optical response. Although the
 233 material is highly anisotropic ($m_{32} \neq 0$), its random growth results in overall isotropic behavior

234 (average $m_{32} = 0$). The full Mueller Matrix is in Supplementary note 3. The red curve in panel (i)
235 is a Gaussian fit. **k** Optical constants of PdSe₂ in the broad spectral range 0.124 – 6 eV (200 –
236 10000 nm). For PdSe₂ optical model, see Supplementary Note 4. Interestingly, the excitonic
237 peaks of PdSe₂ coincide with the Fabry-Perot resonances of SiO₂ (280 nm)/Si.

238 **Applications of topological zeros: sensing**

239 Simple planar structures studied here are easy to incorporate and leverage in industrial and
240 scientific devices where the optical phase plays a critical role.^{5,24,25,31,44} The most prominent
241 practical examples are holography,^{24,25,44} image processing^{45,46}, label-free bio- or chemical
242 sensing,⁴⁷⁻⁵⁰ and quantum key distribution.^{51,52} To validate the concept, we demonstrated that the
243 liquid/PdSe₂/SiO₂/Si system is already an ultrahigh sensitive sensor owing to rapid phase change
244 around the topological point. Note that for sensing measurements we used ellipsometer in the
245 most accurate nulling mode (Methods) and 7.1 nm PdSe₂ thin film to have topological zero in the
246 operation range of our device since liquid changes zero's spectral and angle position according
247 to Equations (2-3).

248 For demonstration, we used water with 0, 2.5, 5, 15, and 20 % volume concentration of
249 isopropanol. Notably, the measured Ψ and Δ in water are in agreement with the predicted values
250 (see Supplementary Note 5) whereby confirming the water stability of PdSe₂ in addition to its
251 recently shown air stability.⁴⁰ Then, to alter the refractive index (RI), we injected isopropanol
252 into the solution and recorded Ψ and Δ (Figure 4a-b) for each water solution. As predicted, the
253 change in amplitude response, Ψ , (Figure 4a and c) is relatively small due to the resonance's
254 topological nature, whereas Δ (Figure 4b and d) shows a dramatic dependence on RI of liquid.
255 Noteworthy, the phase sensitivity in our device of $7.5 \cdot 10^4$ degrees per refractive index unit
256 (deg/RIU) exceeds that of the cutting-edge sensor based on plasmonic surface lattice resonance
257 with $5.7 \cdot 10^4$ deg/RIU.³¹ Therefore, the investigated system PdSe₂/SiO₂/Si is already a ready-to-
258 use scalable device with outstanding performance thanks to the pronounced phase effect in
259 topological points.



260

261 **Figure 4. Sensor based on topology of PdSe₂ film on SiO₂/Si.** **a, b** The dependence of
 262 ellipsometric parameters Ψ (amplitude) and Δ (phase) on the refractive index (RI) of the
 263 investigated liquid recorded at the incidence angle $\theta = 49.4^\circ$, corresponding to the topological
 264 zero. **c** Spectral shift of the resonance position of Ψ spectrum with the change of the medium RI.
 265 **d** The maximum phase shift of the measured spectra with respect to the media with RI = 1.35
 266 (water). The inset shows the phase shift of the measured spectra with respect to the media with
 267 RI = 1.35 (water).

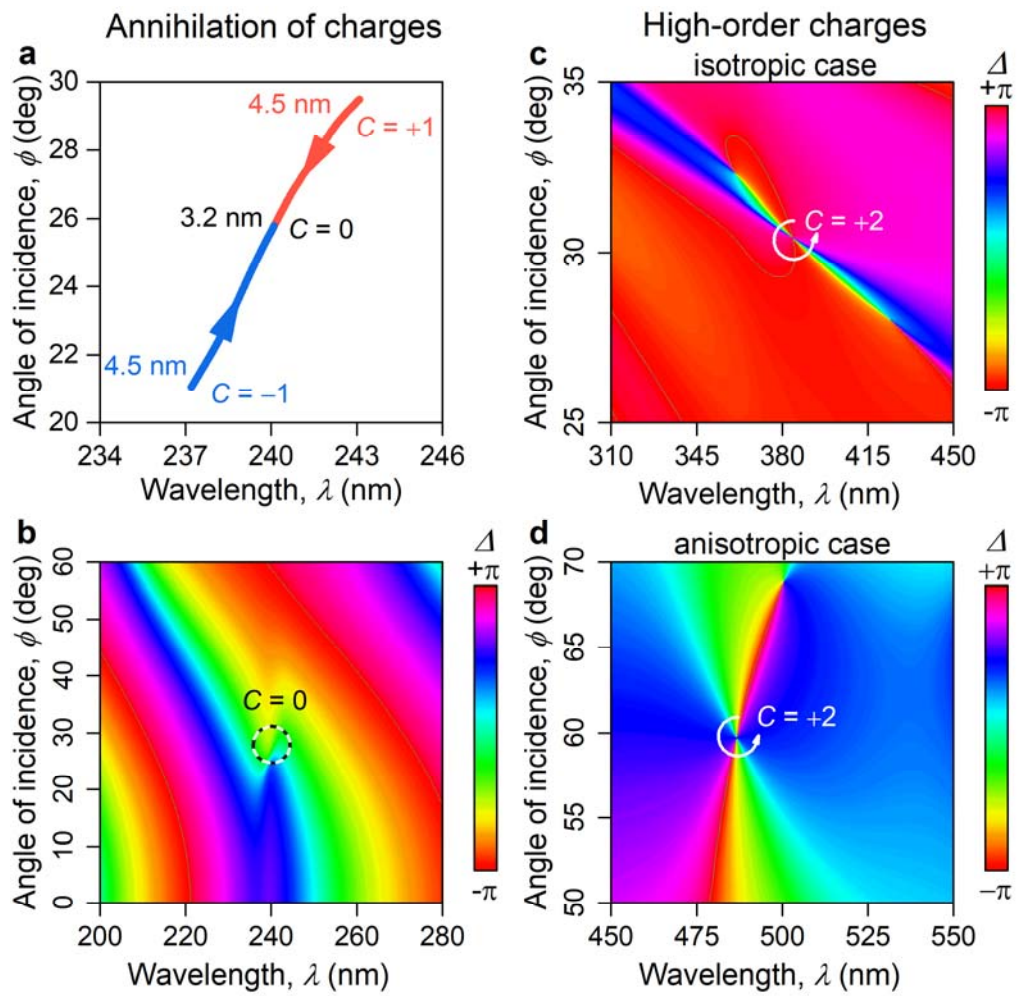
268 **Evolution of phase singularities**

269 So far we have considered and observed reflection phase singularities with unitary topological
270 charge, wherein the argument makes a $\pm 2\pi$ round-trip around the singularity. These points,
271 however, are not stationary and evolve with the material parameters, as Equations (2-3) suggest.
272 When two points with opposite charges (+1 and -1) meet in the parameter space, they annihilate
273 leaving no phase singularity. We theoretically observe such annihilation with variation of the
274 PdSe₂ film thickness, t , when two phase singularities with opposite topological charges meet at
275 around $t \approx 3.2$ nm (Figure 5a). This case happens when the material dispersion curve in Figure
276 5b becomes tangent to zero-reflection surface. The corresponding angle-resolved spectrum of Δ
277 shown in Figure 5b plotted for $t = 3.2$ nm reveals the absence of any phase singularities.
278 Therefore, by varying the thickness one is able to control the position and amount of phase
279 singularities, which appear or disappear in pairs, so that the total topological charge preserves.

280 Next, we examine the possibility of phase singularities with higher topological charges, $|C| >$
281 1. One potential opportunity for the emergence of a non-unitary topological charge is when a
282 phase singularity either in r_p or r_s exhibits a non-unitary charge. Unfortunately, for non-magnetic
283 materials in a planar system, zeros in r_p or r_s are essentially non-degenerate (Supplementary
284 Note 6).

285 However, since ρ is the ratio of two reflection coefficients, another possibility is when a
286 $C = \pm 1$ phase singularity of r_s coincides in the parameter space with a $C = \mp 1$ phase singularity
287 of r_p . This gives rise to a $C = \pm 2$ phase singularity of ρ , which can be detected by spectroscopic
288 ellipsometry. Equating the right-hand sides of Equations (2) and (3), we obtain an equation that
289 determines, for a given substrate, the position of the point at which the zero-reflection conditions
290 for both polarizations coincide; then we can immediately calculate the dielectric constant of the
291 film that satisfies this condition. The charge of a point is determined by the derivative of the
292 material dispersion curve, so the last step is to choose the direction of the material dispersion
293 curve near the zero-reflection point. By using the set of parameters satisfying these conditions

294 (Supplementary Note 6), we observe a $C = +2$ phase singularity in the spectrum of ρ , Figure
 295 5c. The use of in-plane anisotropy can significantly assist in the design of non-unitary charged
 296 points of ρ . Suppose the main optical axis of the film is oriented along with the in-plane
 297 component of the wave vector, then the p-polarization is affected by only the longitudinal
 298 component of the permittivity and the s-polarization only by the transverse one. In that case, it is
 299 possible to select zero-reflection conditions for different polarizations entirely independently.
 300 Therefore, in contrast to isotropic materials, for which the position of points with a topological
 301 double charge depends on the properties of the substrate, in the case of in-plane anisotropic
 302 materials, it is potentially possible to obtain a point with $C = \pm 2$ at any point in the space of
 303 angles and frequencies (see Supplementary Note 7). One of such cases is shown in Figure 5d.



304

305 **Figure 5. Topological effects in phase singularities. a, b** The parameter change, here the
306 thickness of PdSe₂, alters the positions of topological points, resulting, at specific thickness ($t =$
307 3.2 nm), in annihilation of opposite topological charges. **c, d** Topological charges with $C = +2$
308 for ellipsometric phase Δ with isotropic and anisotropic thin films with system's parameters
309 collected in Supplementary Note 7.

310 For $C = \pm 2$ singularities demonstrated in Figure 5c-d, the phase makes a $\pm 4\pi$ round-trip
311 around such a singularity, thus increasing the local phase gradient approximately by a factor of
312 two, which could significantly improve phase applications. For instance, the sensitivity of the
313 corresponding refractive index sensor may increase approximately two-fold.

314 The scenario of non-unitary phase singularities is somewhat reminiscent of exceptional points
315 in non-Hermitian optical systems.⁵³ Such points, which correspond to coalescent eigenstates of a
316 non-Hermitian Hamiltonian, feature a strong $(\epsilon - \epsilon_0)^{1/(N+1)}$ dependence of the eigenenergies of
317 the optical system on a perturbation parameter ϵ in the vicinity of the exceptional point ϵ_0 (with
318 N being the order of the exceptional point), which has been used for boost the sensitivity.

319 Additionally, upon appropriate engineering of the system the same concept of topological
320 phase manipulation could also be applied in transmission regime, thus bridging our phase
321 engineering approach with metasurfaces.

322 **DISCUSSION**

323 Flat optics enable the design of optical components into thin, planar, and CMOS-compatible
324 structures. Coupled with 2D materials, it evolves into 2D flat optics with ultracompact and
325 tunable devices. Nevertheless, atomically thin optical elements suffer from low efficiency of
326 phase manipulation. To lift this limitation and achieve phase control with 2D materials, we
327 utilized topologically protected zeros of a simple heterostructure. We showed both
328 experimentally and theoretically that a whole set of high-index 2D materials could provide rapid
329 phase variations revealed by spectroscopic ellipsometry. In addition, we demonstrate that

330 topological approach leads to high-performance devices on the sensing example and propose the
331 future direction of topological phase effects such as annihilation and high-order charges. From a
332 broader perspective, our results open new avenues for effective application of atomically thin
333 high-refractive-index materials as phase materials in photonics.

334 **ACKNOWLEDGMENTS**

335 G.E., K.V., D.G.B., G.T., D.Y., S.N., A.V., A.M., I.K., A.A., and V.V. gratefully
336 acknowledges the financial support from the Ministry of Science and Higher Education of the
337 Russian Federation (Agreement No. 075-15-2021-606). A.N.G. acknowledge EU Graphene
338 Flagship, Core 3 (881603).

339 **AUTHOR CONTRIBUTIONS**

340 [†]These authors contributed equally. A.N.G., V.V., K.S.N., V.K., and A.A. suggested and
341 directed the project. G.E., V.K., G.T., Y.S., D.Y., S.N., S.Z., R.R., and A.M.M. performed the
342 measurements and analyzed the data. K.V., D.G.B., G.E., A.M., I.K., and A.V. provided
343 theoretical support. G.A.E., K.V., and D.G.B. wrote the original manuscript. G.E., K.V., D.G.B.,
344 A.N.G., K.S.N., V.V., and A.A. reviewed and edited the paper. All authors contributed to the
345 discussions and commented on the paper.

346 **COMPETING INTERESTS**

347 The authors declare no competing interests.

348 **METHODS**

349 **Ellipsometry measurements.** For visualization of topological charge in phase, we used a
350 variable-angle spectroscopic ellipsometer (VASE, J.A. Woollam Co.) since it measures
351 amplitude and phase of complex reflection ratio simultaneously. Measurements were done over a
352 wide wavelength range from 248 to 1240 nm (1 – 5 eV) in steps of 1 nm and multiple angles of
353 incidence in the range 15-80° with 0.5° step. Ellipsometer has a single chamber monochromator

354 with two gratings: 1200 g/mm for visible light (248 – 1040 nm) with 4.6 nm bandwidth and 600
355 g/mm for near-infrared interval (1040 – 1240 nm) with 9.2 nm bandwidth.

356 For accurate refractive index sensing, we performed the nulling ellipsometry with Accurion
357 nanofilm_ep4 ellipsometer. During the measurement light was initially directed through the
358 polarizer then through the compensator, whose settings were adjusted until the reflection from
359 the sample became linearly polarized. Afterward, the analyzer was set to achieve the minimum
360 in the signal at the photodetector. The final positions of polarizer and analyzer at signal's
361 minimum uniquely define ellipsometric parameters Ψ and Δ . Measurements were done over a
362 wavelength range from 300 to 360 nm in steps of 0.1 nm with 4 nm bandwidth and at 49.4°
363 incident angle corresponding to the singular point of PdSe₂ in water.

364 To probe anisotropic response, we also measured 11 elements of Mueller Matrix (m_{12} , m_{13} , m_{21} ,
365 m_{22} , m_{23} , m_{24} , m_{31} , m_{32} , m_{33} , m_{34}) on Accurion nanofilm_ep4 ellipsometer over 400 – 1000 nm
366 wavelength range in 5 nm step with 4 nm bandwidth at 50° incident angle in a rotation
367 compensator mode to get access to Stokes parameters in the input branch of ellipsometer.

368 **Optical visualization.** The surface images (2400 × 2400 pixels) of PdSe₂ were captured by an
369 optical microscope (Nikon LV150L) with a digital camera DS-Fi3.

370 **Atomic force microscopy.** The thickness and surface morphology of the PdSe₂ film were
371 accurately characterized by an atomic force microscope (AFM, NT-MDT Spectrum Instruments
372 “Ntegra”) using AFM in a peak-force mode at ambient conditions. AFM measurements were
373 carried out using cantilever tips from NT-MDT (ETALON, HA_NC) with a spring constant of
374 3.5 N/m, a tip radius < 10 nm and a resonant frequency of 140 kHz. Images of PdSe₂ surface
375 were taken with 512 × 512 pixels and scan rate of 0.5 Hz, after that data were analyzed by
376 Gwyddion software.

377 **Scanning electron microscopy.** Scanning electron microscopy (SEM, JEOL JSM-7001F) with a
378 Schottky emitter in secondary electron imaging mode with a voltage of 30 kV and current of

379 67 μA , and a working distance of ~ 6.3 mm was applied to study in detail surface features and
380 homogeneity of the PdSe_2 film surface within different areas using 1960×1280 pixel scan.

381 **XPS characterization.** The chemical states of the elements in the film, as well as the valence
382 band were analyzed by X-ray photoelectron spectroscopy (XPS) in Theta Probe tool (Thermo
383 Scientific) under ultrahigh vacuum conditions (base pressure $< 10^{-9}$ mBar) with a
384 monochromatic Al-K_α X-ray source (1486.6 eV). Photoelectron spectra were acquired using
385 fixed analyzer transmission (FAT) mode with 50 eV pass energy. The spectrometer energy scale
386 was calibrated on the $\text{Au } 4f_{7/2}$ line (84.0 eV).

387 **X-ray diffraction.** X-ray powder diffractometer (XRD, Thermo ARL X'TRA) equipped with
388 $\text{Cu K}\alpha$ radiation $\lambda = 0.154$ nm was used to characterize the crystalline structure and phase of
389 PdSe_2 film. The XRD pattern was taken at ambient conditions by 2θ -scan over the range of 20–
390 75° with a step of 0.05° and accumulation time of 2 s.

391 **Reflectance measurements.** Fourier-transform spectrometer Bruker Vertex 80v has been used
392 to measure the reflection coefficient at the normal incident at room temperature in the frequency
393 range from 1000 to 24000 cm^{-1} , as the reference was used the reflection from the gold mirror.

394 **Raman characterization.** The experimental setup used for Raman measurements was a
395 confocal scanning Raman microscope Horiba LabRAM HR Evolution (HORIBA Ltd., Kyoto,
396 Japan). All measurements were carried out using linearly polarized excitation at wavelengths
397 532 and 632.8 nm, 1800 lines/mm diffraction grating, and $\times 100$ objective (N.A. = 0.90), whereas
398 we used un-polarized detection to have a significant signal-to-noise ratio. The spot size was
399 approximately $0.43\mu\text{m}$. The Raman images were recorded by mapping the spatial dependence of
400 Raman intensity integrated at the main Raman peaks within the shift range $136 - 156 \text{ cm}^{-1}$, for
401 each of the 45×45 points in the scan, with an integration time of 500 ms at each point and
402 incident power $P = 1.7 \text{ mW}$.

403 **DATA AVAILABILITY**

404 The datasets generated during and/or analyzed during the current study are available from the
405 corresponding author on reasonable request.

406

407 REFERENCES

- 408 1. Yu, N. *et al.* Light Propagation with Phase Discontinuities: Generalized Laws of
409 Reflection and Refraction. *Science* **334**, 333–337 (2011).
- 410 2. Deng, Z.-L. & Li, G. Metasurface optical holography. *Mater. Today Phys.* **3**, 16–32
411 (2017).
- 412 3. Jung, C. *et al.* Near-zero reflection of all-dielectric structural coloration enabling
413 polarization-sensitive optical encryption with enhanced switchability. *Nanophotonics* **10**,
414 919–926 (2020).
- 415 4. Grigorenko, A. N., Nikitin, P. I. & Kabashin, A. V. Phase jumps and interferometric
416 surface plasmon resonance imaging. *Appl. Phys. Lett.* **75**, 3917–3919 (1999).
- 417 5. Kravets, V. G. *et al.* Singular phase nano-optics in plasmonic metamaterials for label-free
418 single-molecule detection. *Nat. Mater.* **12**, 304–309 (2013).
- 419 6. Malassis, L. *et al.* Topological Darkness in Self-Assembled Plasmonic Metamaterials.
420 *Adv. Mater.* **26**, 324–330 (2014).
- 421 7. Hein, S. M. & Giessen, H. Retardation-induced phase singularities in coupled plasmonic
422 oscillators. *Phys. Rev. B* **91**, 205402 (2015).
- 423 8. Kravets, V. G., Schedin, F. & Grigorenko, A. N. Plasmonic blackbody: Almost complete
424 absorption of light in nanostructured metallic coatings. *Phys. Rev. B* **78**, 205405 (2008).
- 425 9. Kim, S. *et al.* Electronically Tunable Perfect Absorption in Graphene. *Nano Lett.* **18**, 971–
426 979 (2018).
- 427 10. Zhu, L. *et al.* Angle-selective perfect absorption with two-dimensional materials. *Light*
428 *Sci. Appl.* **5**, e16052–e16052 (2016).
- 429 11. Pichler, K. *et al.* Random anti-lasing through coherent perfect absorption in a disordered
430 medium. *Nature* **567**, 351–355 (2019).
- 431 12. Jackson, J. D. Electrodynamics, Classical. in *digital Encyclopedia of Applied Physics*
432 (Wiley-VCH Verlag GmbH & Co. KGaA, 2003).
- 433 13. Baranov, D. G., Edgar, J. H., Hoffman, T., Bassim, N. & Caldwell, J. D. Perfect
434 interferenceless absorption at infrared frequencies by a van der Waals crystal. *Phys. Rev.*
435 *B* **92**, 1–6 (2015).
- 436 14. Sweeney, W. R., Hsu, C. W. & Stone, A. D. Theory of reflectionless scattering modes.
437 *Phys. Rev. A* **102**, 1–20 (2020).
- 438 15. Yan, C., Raziman, T. V. & Martin, O. J. F. Phase Bifurcation and Zero Reflection in
439 Planar Plasmonic Metasurfaces. *ACS Photonics* **4**, 852–860 (2017).
- 440 16. Berkhout, A. & Koenderink, A. F. Perfect Absorption and Phase Singularities in Plasmon
441 Antenna Array Etalons. *ACS Photonics* **6**, 2917–2925 (2019).

- 442 17. Born, M. *et al.* *Principles of Optics*. (Cambridge University Press, 1999).
- 443 18. Kildishev, A. V., Boltasseva, A. & Shalaev, V. M. Planar Photonics with Metasurfaces.
444 *Science* **339**, 1232009–1232009 (2013).
- 445 19. Yu, N. & Capasso, F. Flat optics with designer metasurfaces. *Nat. Mater.* **13**, 139–150
446 (2014).
- 447 20. Gomez-Diaz, J. S. & Alù, A. Flatland Optics with Hyperbolic Metasurfaces. *ACS*
448 *Photonics* **3**, 2211–2224 (2016).
- 449 21. Wang, S. *et al.* A broadband achromatic metalens in the visible. *Nat. Nanotechnol.* **13**,
450 227–232 (2018).
- 451 22. Chen, W. T. *et al.* A broadband achromatic metalens for focusing and imaging in the
452 visible. *Nat. Nanotechnol.* **13**, 220–226 (2018).
- 453 23. Lin, H. *et al.* Diffraction-limited imaging with monolayer 2D material-based ultrathin flat
454 lenses. *Light Sci. Appl.* **9**, 137 (2020).
- 455 24. Zheng, G. *et al.* Metasurface holograms reaching 80% efficiency. *Nat. Nanotechnol.* **10**,
456 308–312 (2015).
- 457 25. Ni, X., Kildishev, A. V. & Shalaev, V. M. Metasurface holograms for visible light. *Nat.*
458 *Commun.* **4**, 2807 (2013).
- 459 26. Yue, Z., Xue, G., Liu, J., Wang, Y. & Gu, M. Nanometric holograms based on a
460 topological insulator material. *Nat. Commun.* **8**, 15354 (2017).
- 461 27. Xia, F., Wang, H., Xiao, D., Dubey, M. & Ramasubramaniam, A. Two-dimensional
462 material nanophotonics. *Nat. Photonics* **8**, 899–907 (2014).
- 463 28. Li, Z. *et al.* Graphene Plasmonic Metasurfaces to Steer Infrared Light. *Sci. Rep.* **5**, 12423
464 (2015).
- 465 29. Mak, K. F. & Shan, J. Photonics and optoelectronics of 2D semiconductor transition metal
466 dichalcogenides. *Nat. Photonics* **10**, 216–226 (2016).
- 467 30. Shi, Y.-L., Zhuo, M.-P., Wang, X.-D. & Liao, L.-S. Two-Dimensional Organic
468 Semiconductor Crystals for Photonics Applications. *ACS Appl. Nano Mater.* **3**, 1080–
469 1097 (2020).
- 470 31. Danilov, A. *et al.* Ultra-narrow surface lattice resonances in plasmonic metamaterial
471 arrays for biosensing applications. *Biosens. Bioelectron.* **104**, 102–112 (2018).
- 472 32. Harland G. Tompkins, J. N. H. *Spectroscopic Ellipsometry Practical Application to Thin*
473 *Film Characterization*. (Momentum Press, 2016).
- 474 33. Passler, N. C. & Paarmann, A. Generalized 4×4 matrix formalism for light propagation
475 in anisotropic stratified media: study of surface phonon polaritons in polar dielectric
476 heterostructures. *J. Opt. Soc. Am. B* **34**, 2128 (2017).
- 477 34. El-Sayed, M. A. *et al.* Optical Constants of Chemical Vapor Deposited Graphene for
478 Photonic Applications. *Nanomaterials* **11**, 1230 (2021).
- 479 35. Ermolaev, G. A., Yakubovsky, D. I., Stebunov, Y. V., Arsenin, A. V. & Volkov, V. S.
480 Spectral ellipsometry of monolayer transition metal dichalcogenides: Analysis of
481 excitonic peaks in dispersion. *J. Vac. Sci. Technol. B* **38**, 014002 (2020).
- 482 36. Sreekanth, K. V. *et al.* Biosensing with the singular phase of an ultrathin metal-dielectric

- 483 nanophotonic cavity. *Nat. Commun.* **9**, 369 (2018).
- 484 37. Lu, L., Joannopoulos, J. D. & Soljačić, M. Topological photonics. *Nat. Photonics* **8**, 821–
485 829 (2014).
- 486 38. Zeng, L. H. *et al.* Controlled Synthesis of 2D Palladium Diselenide for Sensitive
487 Photodetector Applications. *Adv. Funct. Mater.* **29**, 1–9 (2019).
- 488 39. Zhang, G. *et al.* Optical and electrical properties of two-dimensional palladium diselenide.
489 *Appl. Phys. Lett.* **114**, (2019).
- 490 40. Oyedele, A. D. *et al.* PdSe₂: Pentagonal Two-Dimensional Layers with High Air Stability
491 for Electronics. *J. Am. Chem. Soc.* **139**, 14090–14097 (2017).
- 492 41. Yu, J. *et al.* Direct Observation of the Linear Dichroism Transition in Two-Dimensional
493 Palladium Diselenide. *Nano Lett.* **20**, 1172–1182 (2020).
- 494 42. Ermolaev, G. A. *et al.* Giant optical anisotropy in transition metal dichalcogenides for
495 next-generation photonics. *Nat. Commun.* **12**, 854 (2021).
- 496 43. Kuklin, A. V. & Ågren, H. Quasiparticle electronic structure and optical spectra of single-
497 layer and bilayer PdSe₂: Proximity and defect-induced band gap renormalization. *Phys.*
498 *Rev. B* **99**, 245114 (2019).
- 499 44. Wang, Y. *et al.* Atomically Thin Noble Metal Dichalcogenides for Phase-Regulated Meta-
500 optics. *Nano Lett.* **20**, 7811–7818 (2020).
- 501 45. Zhu, T. *et al.* Topological optical differentiator. *Nat. Commun.* **12**, 680 (2021).
- 502 46. Huo, P. *et al.* Photonic Spin-Multiplexing Metasurface for Switchable Spiral Phase
503 Contrast Imaging. *Nano Lett.* **20**, 2791–2798 (2020).
- 504 47. Grigorenko, A. *et al.* Dark-field surface plasmon resonance microscopy. *Opt. Commun.*
505 **174**, 151–155 (2000).
- 506 48. Kravets, V. G., Schedin, F., Kabashin, A. V. & Grigorenko, A. N. Sensitivity of collective
507 plasmon modes of gold nanoresonators to local environment. *Opt. Lett.* **35**, 956 (2010).
- 508 49. Wu, F. *et al.* Layered material platform for surface plasmon resonance biosensing. *Sci.*
509 *Rep.* **9**, 20286 (2019).
- 510 50. Kabashin, A. V. *et al.* Phase-Responsive Fourier Nanotransducers for Probing 2D
511 Materials and Functional Interfaces. *Adv. Funct. Mater.* **29**, 1902692 (2019).
- 512 51. Hiskett, P. A. *et al.* Long-distance quantum key distribution in optical fibre. *New J. Phys.*
513 **8**, 193–193 (2006).
- 514 52. Takesue, H. *et al.* Quantum key distribution over a 40-dB channel loss using
515 superconducting single-photon detectors. *Nat. Photonics* **1**, 343–348 (2007).
- 516 53. Özdemir, Ş. K., Rotter, S., Nori, F. & Yang, L. Parity–time symmetry and exceptional
517 points in photonics. *Nat. Mater.* **18**, 783–798 (2019).
- 518

Supplementary Files

This is a list of supplementary files associated with this preprint. Click to download.

- [SupplementaryInformationNatComm.pdf](#)